
This is an electronic reprint of the original article.
This reprint may differ from the original in pagination and typographic detail.

Jose, Miguel Luque Raigon; Halme, Janne; Carmen, Lopez Lopez
Angular optical behavior of photonic-crystal-based dye-sensitized solar cells

Published in:
Journal of Photonics for Energy

DOI:
[10.1117/1.JPE.9.025501](https://doi.org/10.1117/1.JPE.9.025501)

Published: 01/04/2019

Document Version
Publisher's PDF, also known as Version of record

Please cite the original version:
Jose, M. L. R., Halme, J., & Carmen, L. L. (2019). Angular optical behavior of photonic-crystal-based dye-sensitized solar cells. *Journal of Photonics for Energy*, 9(2), 1-18. Article 025501.
<https://doi.org/10.1117/1.JPE.9.025501>

This material is protected by copyright and other intellectual property rights, and duplication or sale of all or part of any of the repository collections is not permitted, except that material may be duplicated by you for your research use or educational purposes in electronic or print form. You must obtain permission for any other use. Electronic or print copies may not be offered, whether for sale or otherwise to anyone who is not an authorised user.

Journal of Photonics for Energy

PhotonicsforEnergy.SPIEDigitalLibrary.org

Angular optical behavior of photonic-crystal-based dye-sensitized solar cells

José Miguel Luque-Raigón
Janne Halme
Carmen López-López

SPIE.

José Miguel Luque-Raigón, Janne Halme, Carmen López-López, "Angular optical behavior of photonic-crystal-based dye-sensitized solar cells," *J. Photon. Energy* **9**(2), 025501 (2019), doi: 10.1117/1.JPE.9.025501.

Angular optical behavior of photonic-crystal-based dye-sensitized solar cells

José Miguel Luque-Raigón,^{a,*} Janne Halme,^{a,*} and Carmen López-López^b

^aAalto University School of Science, Department of Applied Physics, Espoo, Finland

^bInstituto de Ciencia de Materiales de Sevilla (Consejo Superior de Investigaciones Científicas—Universidad de Sevilla), Seville, Spain

Abstract. Theoretical modeling of the incidence angle dependence is important for the performance evaluation of solar cells especially when they employ structural photonics that enhance their aesthetics for building-integrated photovoltaic applications. We present an optical model based on transfer matrix method, which is tailored for the analysis of the angular optical characteristics of dye-sensitized solar cells (DSSC) that incorporate a porous one-dimensional photonic-crystal (1DPC) back reflector. We provide complete mathematical description of the angular optics and electromagnetic energetics of DSSC, including solutions that avoid numerical instabilities in the case of thick, strongly light-absorbing layers. The model showed excellent quantitative agreement with angle-dependent spectral transmittance measurements recorded from complete DSSCs, allowing detailed analysis of the light harvesting enhancement by the dye provided by back-reflection of light from the 1DPC. Determining the ratio of the device transmittance measured with and without a 1DPC is proposed as a simple and practical way to determine the internal reflectance of the 1DPC embedded in the device structure. The reported model provides an accurate description of the coherent angular optics of DSSCs, applicable for situations where light scattering in the device structure can be neglected. © 2019 Society of Photo-Optical Instrumentation Engineers (SPIE) [DOI: [10.1117/1.JPE.9.025501](https://doi.org/10.1117/1.JPE.9.025501)]

Keywords: multiscale vectorial model; transfer matrix method; angular simulation; dye-sensitized solar cell; building-integrated photovoltaics.

Paper 18129 received Nov. 10, 2018; accepted for publication Apr. 11, 2019; published online May 3, 2019.

1 Introduction

The energy conversion efficiency and nominal power rating of photovoltaic (PV) modules are determined for normal incidence of light. However, due to the daily and seasonal variation in the Sun's path in the sky and the fixed orientation and tilt used in most PV installations, sunlight rarely hits solar modules at normal incidence in practical conditions, which causes angular optical losses. Simulation models used for the design and analysis of PV systems account for these angular losses with an incidence angle modifier (IAM) that describes the decrease in light transmission through the front air–glass interface of the module based on Fresnel's equations or generalized empirical relations derived from optical characterization of solar cells.^{1,2} According to theoretical simulations, the annual angular losses in PV energy production are 3% to 8% in Europe, depending on the location and tilt angle, being highest for vertical (facade) installations.¹ Knowing the angle dependence of the module performance is, therefore, important for accurate predictive design and analysis of PV systems.

Optical angular effects are particularly pronounced in solar cells and modules that employ advanced photonic designs to improve both their efficiency and aesthetics. An interesting example is dielectric nanostructures that give spectrally selective reflection that is often strongly angle-dependent. These so-called structural colors have been demonstrated recently for dye-sensitized,^{3–5} organic,⁶ perovskite,⁷ amorphous silicon,⁸ CIGS,⁹ and crystalline silicon solar cells,^{10,11} in view of their potential applications in building-integrated photovoltaics. The

*Address all correspondence to José Miguel Luque-Raigón, E-mail: jmluque@us.es; Janne Halme, E-mail: janne.halme@aalto.fi

angle-dependent optical transmittance and reflectance of this type of solar cells can be subtle functions of their structural properties and differ significantly from the commonly assumed IAM models, which makes theoretical optical modeling an essential tool for their systematic design and optimization.

In this work, we focused on dye-sensitized solar cells (DSSC) equipped with a porous one-dimensional photonic crystal (1DPC).^{4,12–17} The porous 1DPC consists of alternating thin layers of colloidal TiO_2 and SiO_2 particles stacked on top of each other to form a dielectric optical multilayer that acts as a distributed Bragg reflector at the back of the photoelectrode (Fig. 1). The 1DPC layer serves as an optical back-reflector that increases light absorption in the photoelectrode while preserving its semitransparency and allowing ionic diffusion through itself. At the same time, the intense wavelength-selective reflection produced by the 1DPC layer gives rise to structural coloration of the DSSC, which may be used as an additional design factor when searching for a compromise between visible transparency, color, and PV performance of the cells.

Previous works on the 1DPC-DSSC have shown that the peak wavelength and intensity of the 1DPC reflectance for normal incidence depends on the number and thickness of its TiO_2 and SiO_2 layers, and their effective refractive indices, as one would expect for a distributed Bragg reflector.^{13,17,18} Furthermore, López-López et al.^{13,15} studied the angular response of 1DPC-DSSCs through transmittance measurements and found that the 1DPC enhanced the short-circuit photocurrent density of the cells over a broad range of wavelengths (400 to 750 nm) and for all measured incident angles (0 deg to 60 deg). Angular transmittance and photocurrent results were reported also by Anaya et al.¹⁴ However, these works did not pursue detailed theoretical analysis of the observed angular optical characteristics, which would be helpful for systematic development and optimization of 1DPC-DSSCs.

We, therefore, report here a detailed angular optical model of DSSCs based on transfer matrix method (TMM) and verify it quantitatively against angle-dependent optical measurements taken from complete DSSCs, with and without 1DPC layer. We then apply the model to the investigation of angular optical characteristics of 1DPC-DSSCs and propose a simple experimental approach to obtain information on the angle-dependent reflectance spectrum of the 1DPC layer embedded inside the device. This is the first time that a detailed optical TMM model has been applied to the angular optical analysis of 1DPC-DSSC devices with quantitatively comparison with angular optical measurements. The TMM model provides an accurate optical description of the angular characteristics of DSSCs in the case when light scattering effects are negligible, completing our earlier theoretical works on the topic.^{18–20}

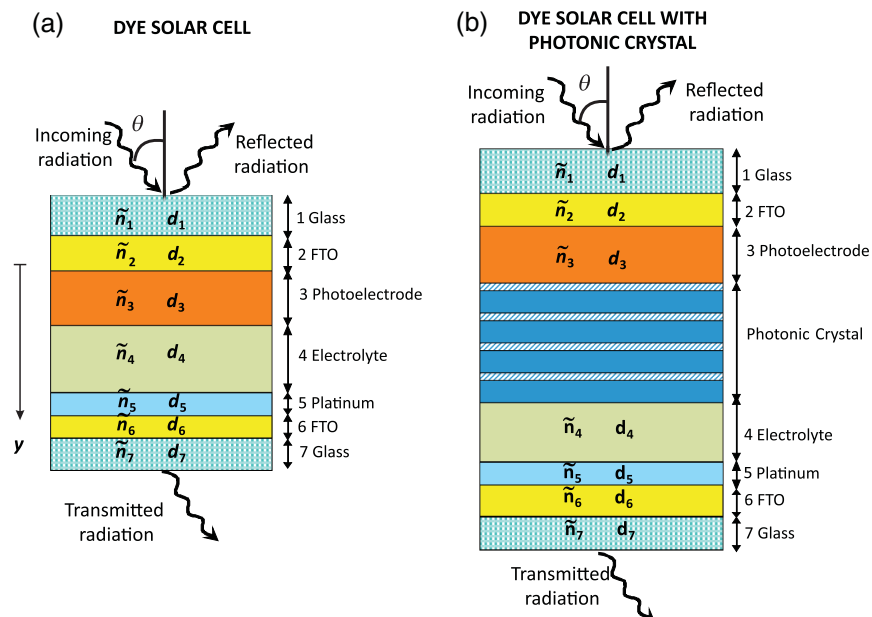


Fig. 1 Structure of the (a) DSSC and (b) 1DPC-DSSC. The refractive indices and thicknesses of the layers are listed in Table 1.

We begin with theoretical description of the model and specification of model parameters in Sec. 2, followed by comparison with experimental results and their discussion in Sec. 3.

2 Theoretical Model and Parameters

2.1 Interaction of Light with 1DPC-DSSC

The interaction of light with the 1DPC-DSSC is described by free-charge Maxwell's equations with the boundary conditions defined by the geometry (Fig. 1). This consists of a finite 1-D nonperiodic multilayer, with $j = 1, 2, \dots, n$ layers with thickness d_j , sandwiched between two external, nonabsorptive, semi-infinite media of air $j = 0, n + 1$. The layers and external media are named regions, and they are bordered by interfaces. The regions are homogeneous, isotropic, linear, and frequency-dependent ω being defined by a complex refractive index $\tilde{n}_j(\omega) \equiv c\tilde{\mathbf{k}}_j(\omega)/\omega$, where the real part describes dispersion and the imaginary part absorption. The frequency is related to the vacuum wavelength λ by the relation $\omega = 2\pi c/\lambda$, where c is the speed of light. The model input parameters are the (effective) complex refractive index $\tilde{n}_j(\lambda) = n_j(\lambda) + i\kappa_j(\lambda) = n_j(\lambda) + i\lambda\alpha_j(\lambda)/4\pi$ and thickness d_j for each layer j . Here $n_j(\lambda)$ is the real refractive index, $\kappa_j(\lambda)$ is the imaginary refractive index, and $\alpha_j(\lambda)$ is the absorption coefficient. Note that the absorption coefficient is a different quantity to the complex wavevector tangent component $\tilde{\alpha}$ introduced later. The absorption processes indicate a dissipative system that is time-irreversible. We consider only ballistic wave propagation because light scattering is weak in our structures. The time-independent solution for the electric field waves is given by $\tilde{\mathbf{E}}_j(\mathbf{r}, t) = \tilde{\mathbf{E}}_j(\mathbf{r})e^{i\omega t}$, where $j = 0, 1, 2, \dots, n, n + 1$ and the imaginary unit is defined as $i = \sqrt{-1}$. Depending on the incident angle, this solution is split at the interfaces to an s-polarized component, also called the transversal electric (TE) mode $\tilde{\mathbf{E}}_j^s(\mathbf{r}, t)$, and to the p-polarized component, called the transversal magnetic (TM) mode $\tilde{\mathbf{E}}_j^p(\mathbf{r}, t)$ (Fig. 2). Additionally, each mode is separated to a forward $\tilde{\mathbf{E}}_j^{s+}(\mathbf{r}, t)$, $\tilde{\mathbf{E}}_j^{p+}(\mathbf{r}, t)$ and backward $\tilde{\mathbf{E}}_j^{s-}(\mathbf{r}, t)$, $\tilde{\mathbf{E}}_j^{p-}(\mathbf{r}, t)$ moving waves, which considers the multiple reflections from all the interfaces of the multilayer. The frequency-dependent wavevector $\tilde{\mathbf{k}}_j(\omega)$ with $j = 0, 1, \dots, n, n + 1$ is projected along y axis and x axis, respectively, as $\tilde{\mathbf{k}}_j(\omega) = \tilde{\beta}_j(\omega)\hat{\mathbf{y}} + \tilde{\alpha}(\omega)\hat{\mathbf{x}} \equiv \tilde{\mathbf{k}}_j(\omega)\{\cos(\tilde{\theta}_j)\hat{\mathbf{y}} + \sin(\tilde{\theta}_j)\hat{\mathbf{x}}\}$, where $\tilde{\theta}_j$ is the complex angle defined between the normal direction to the multilayer $\hat{\mathbf{y}}$ and the corresponding complex wavevector $\tilde{\mathbf{k}}_j(\omega)$ (Fig. 2). The complex wavevector components $\tilde{\beta}_j = \tilde{\beta}_j(\omega)$, $\tilde{\alpha} = \tilde{\alpha}(\omega)$ fulfill the conditions $\text{Im}(\tilde{\beta}_j) \leq 0$, $\text{Im}(\tilde{\alpha}) \leq 0$ where $\text{Im}(\cdot)$ is the imaginary part of the argument.

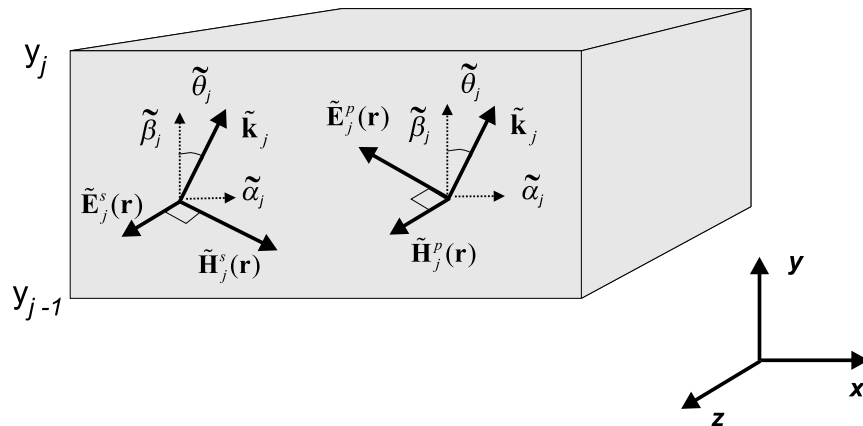


Fig. 2 Vectorial electromagnetic wave propagation in one layer or external media $j = 0, 1, \dots, n, n + 1$ of the multilayer system. The propagating waves consist of two modes: (a) the TE or s-polarization and (b) the TM or p-polarization. The propagation of each mode contains both forward and backward directions (not marked in this figure). Furthermore, each propagation direction contains the multiple reflections generated in the other interfaces of the multilayer.

2.2 Transfer Matrix Method

The TMM^{21–23} is an iterative process that solves the electromagnetic interaction in the multilayer by means of transfer functions. It describes how both the forward and backward wave propagations are affected by the multiple transmissions and reflections generated at each interface throughout the system. The position-dependent electric field in the TMM representation is given by

$$\tilde{E}(\mathbf{r}) = \begin{cases} (1 \ 1)(\mathbf{P}_0^{-1})_{y-y_0} \begin{pmatrix} 1 \\ \tilde{E}_0^- \end{pmatrix} e^{-i\tilde{\alpha}x} & \text{with } y \in (-\infty, y_0); \quad x \in (x_0, +\infty) \\ (1 \ 1)(\mathbf{P}_j^{-1})_{(y-y_{j-1})} \mathbf{D}_j^{-1} (\mathbf{D}_{j-1} \mathbf{P}_{j-1}^{-1} \mathbf{D}_{j-1}^{-1}) \dots \\ \dots (\mathbf{D}_{j-2} \mathbf{P}_{j-2}^{-1} \mathbf{D}_{j-2}^{-1}) (\mathbf{D}_1 \mathbf{P}_1^{-1} \mathbf{D}_1^{-1}) \mathbf{D}_0 \begin{pmatrix} 1 \\ \tilde{E}_0^- \end{pmatrix} e^{-i\tilde{\alpha}x} \\ = (1 \ 1)(\mathbf{P}_j^{-1})_{(y-y_{j-1})} \begin{pmatrix} \tilde{E}_j^+ \\ \tilde{E}_j^- \end{pmatrix} e^{-i\tilde{\alpha}x} & \text{with } y \in (y_{j-1}, y_j); \quad x \in (x_0, +\infty) \end{cases}, \quad (1)$$

where the amplitude condition $\tilde{E}_{n+1}^- = 0$ means that there are no reflected waves in the outgoing medium, whereas $\tilde{E}_0^+ = 1$ means that the incident wave is normalized to unity. These amplitude conditions and Eq. (1) provide the solution for the unknown electric field amplitudes \tilde{E}_j^+ , \tilde{E}_j^- in each region. The matrices from Eq. (1) are defined as

$$\begin{aligned} \mathbf{P}_j &\equiv \begin{bmatrix} e^{i\tilde{\beta}_j(y_j-y_{j-1})} & 0 \\ 0 & e^{-i\tilde{\beta}_j(y_j-y_{j-1})} \end{bmatrix}; \\ \mathbf{D}_j &\equiv \begin{cases} \begin{bmatrix} 1 & 1 \\ \tilde{n}_j \cos(\tilde{\theta}_j) & -\tilde{n}_j \cos(\tilde{\theta}_j) \end{bmatrix} & \text{s-polarization} \\ \begin{bmatrix} \cos(\tilde{\theta}_j) & \cos(\tilde{\theta}_j) \\ \tilde{n}_j & -\tilde{n}_j \end{bmatrix} & \text{p-polarization} \end{cases} \\ (\mathbf{P}_0)_{y-y_0} &\equiv \begin{bmatrix} e^{i\tilde{\beta}_0(y-y_0)} & 0 \\ 0 & e^{-i\tilde{\beta}_0(y-y_0)} \end{bmatrix}; \\ (\mathbf{P}_j)_{(y-y_{j-1})} &\equiv \begin{bmatrix} e^{i\tilde{\beta}_j(y-y_{j-1})} & 0 \\ 0 & e^{-i\tilde{\beta}_j(y-y_{j-1})} \end{bmatrix}. \end{aligned} \quad (2)$$

Note that the polarization of the propagating wave is given by selecting the dynamic matrix \mathbf{D} [see the definitions in Eq. (2)], which is why the amplitude coefficients are noted generically as \tilde{E}_j^+ , \tilde{E}_j^- . The magnetic field can be evaluated from the electric field [Eq. (1)] using the Maxwell's equations,²⁴ but we are not interested in obtaining it for the purposes of this work.

2.3 Stable Representation of the Transfer Matrix Method

The exponential terms in the TMM representation, Eqs. (1) and (2), give numerical instabilities in some extreme cases, when the inversion of the \mathbf{P} matrices is performed [see definitions in Eq. (2)]. These instabilities can be avoided using the modified TMM that uses reference system transformation to achieve a numerically stable electric field solution.^{19,20} The new electric field is given by

$$\tilde{E}'(\mathbf{r}) = \begin{cases} (1 \ 1)(\mathbf{P}_0^{-1})_{y-y_0} \begin{pmatrix} 1 \\ \tilde{E}_0^- \end{pmatrix} e^{-i\tilde{\alpha}x} & \text{with } y \in (-\infty, y_0); \quad x \in (x_0, +\infty) \\ (1 \ 1) \begin{bmatrix} 1 & 0 \\ 0 & e^{i\sum_{k=1}^{j-1} \tilde{\beta}_k d_k + i\tilde{\beta}_j(y-y_{j-1})} \end{bmatrix} \begin{pmatrix} \tilde{E}_j^+ \\ \tilde{E}_j^- \end{pmatrix} e^{-i\tilde{\alpha}x} & \text{with } y \in (y_{j-1}, y_j); \quad x \in (x_0, +\infty), \end{cases} \quad (3)$$

where $j = 1, \dots, n + 1$. The stable TMM for the electric field $\tilde{E}'(\mathbf{r})$ of Eq. (3) is employed to build up the original electric field $\tilde{E}(\mathbf{r})$ through the following relations:

$$\begin{aligned} \tilde{E}_j(\mathbf{r}) &= \mathbf{M}_{j-1}^+ \tilde{E}'_j(\mathbf{r}) \quad \text{with } y \in (y_{j-1}, y_j); \quad x \in (x_0, +\infty) \quad \text{where} \\ \tilde{E}_j(\mathbf{r}) &= \begin{bmatrix} e^{-i\tilde{\beta}_j(y-y_{j-1})} & 0 \\ 0 & e^{+i\tilde{\beta}_j(y-y_{j-1})} \end{bmatrix} \begin{pmatrix} \tilde{E}_j^+ \\ \tilde{E}_j^- \end{pmatrix} e^{-i\tilde{\alpha}x}; \\ \tilde{E}'_j(\mathbf{r}) &= \begin{bmatrix} 1 & 0 \\ 0 & e^{i\sum_{k=1}^{j-1} \tilde{\beta}_k d_k + i\tilde{\beta}_j(y-y_{j-1})} \end{bmatrix} \begin{pmatrix} \tilde{E}_j^+ \\ \tilde{E}_j^- \end{pmatrix} e^{-i\tilde{\alpha}x}; \quad \mathbf{M}_0^+ = \begin{pmatrix} 1 & 0 \\ 0 & 1 \end{pmatrix}; \\ \mathbf{M}_1^+ &= \begin{pmatrix} e^{-i\sum_{k=1}^1 \tilde{\beta}_k d_k} & 0 \\ 0 & e^{-i\sum_{k=1}^1 \tilde{\beta}_k d_k} \end{pmatrix}; \dots; \mathbf{M}_{j-1}^+ = \begin{pmatrix} e^{-i\sum_{k=1}^{j-1} \tilde{\beta}_k d_k} & 0 \\ 0 & e^{-i\sum_{k=1}^{j-1} \tilde{\beta}_k d_k} \end{pmatrix}, \end{aligned} \quad (4)$$

where $j = 1, \dots, n + 1$. This calculation scheme of Eqs. (3) and (4) generates the same electric field $\tilde{E}(\mathbf{r}, t)$ as the scheme of Eqs. (1) and (2), but with the difference that Eqs. (3) and (4) are fully stable in the numerical calculations. This proposed theoretical scheme is tailored to be used in 1-D optical structures. Nevertheless, the same theory can be applied for 2-D and 3-D structures using the local density of states, where band structure is characterized by the 2-D and 3-D geometry of the structure.^{25,26}

2.4 Total Reflectance, Transmittance, and Absorptance of the Solar Cell

The two TMM representations given in Secs. 2.2 and 2.3 give the same analytical solution for the total reflectance, total absorptance, and total transmittance of the 1DPC-DSSC, which is summarized as

$$\begin{pmatrix} \tilde{E}_{n+1}^+ \\ 0 \end{pmatrix} = \mathbf{D}_{n+1}^{-1} (\mathbf{D}_n \mathbf{P}_n^{-1} \mathbf{D}_n^{-1}) (\mathbf{D}_{n-1} \mathbf{P}_{n-1}^{-1} \mathbf{D}_{n-1}^{-1}) \dots (\mathbf{D}_1 \mathbf{P}_1^{-1} \mathbf{D}_1^{-1}) \mathbf{D}_0 \begin{pmatrix} 1 \\ \tilde{E}_0^- \end{pmatrix}, \quad (5)$$

where dynamic matrices are defining two interfaces $0 \leftrightarrow 1$ and $n \leftrightarrow n + 1$, which represent the physical boundaries of the 1DPC-DSSC. Therefore, the TMM defined in Eq. (5) provides the total reflectance in $0 \leftrightarrow 1$, the total transmittance in $n \leftrightarrow n + 1$, and the total absorptance between $0 \leftrightarrow 1$ and $n \leftrightarrow n + 1$. In particular, the DSSC of Fig. 1(a) has $n = 7$, whereas the 1DPC-DSSC of Fig. 1(b) has $n = 15$. The transfer matrix \mathbf{M} is defined as

$$\mathbf{M} = \begin{pmatrix} M_{11} & M_{12} \\ M_{21} & M_{22} \end{pmatrix} \equiv \mathbf{D}_{n+1}^{-1} (\mathbf{D}_n \mathbf{P}_n^{-1} \mathbf{D}_n^{-1}) (\mathbf{D}_{n-1} \mathbf{P}_{n-1}^{-1} \mathbf{D}_{n-1}^{-1}) \dots (\mathbf{D}_1 \mathbf{P}_1^{-1} \mathbf{D}_1^{-1}) \mathbf{D}_0. \quad (6)$$

With the normalization defined by $\tilde{E}_{n+1}^- = 0$ (no reflected waves in the outgoing medium) and $\tilde{E}_0^+ = 1$ (the incident wave in the incoming medium is normalized to unity), it is easy to obtain the reflection and transmission coefficients as $r = \tilde{E}_0^-$ and $t = \tilde{E}_{n+1}^+$. The determinant $|\mathbf{M}| = 1$ can be easily evaluated considering that the propagation matrices fulfill $|\mathbf{P}| = 1$, and the external media are the same (air) $\mathbf{D}_{n+1} = \mathbf{D}_0$. In these conditions, the reflection and transmission coefficients depend on the transfer matrix components as follows:

$$r = \tilde{E}_0^- = -M_{21}/M_{22} \quad t = \tilde{E}_{n+1}^+ = 1/M_{22}; \quad (7)$$

the reflectance R , transmittance T , and absorptance A are given by

$$R = |r|^2; \quad T = |t|^2; \quad A = 1 - R - T. \quad (8)$$

This calculation in Eq. (8) is independently evaluated for the s- and p-polarizations, which are represented by the two kinds of dynamic matrices defined in Eq. (2) for both polarizations. Theoretical calculations for the interaction of solar cells with 1DPC have been done by the TMM, and a study of the state of polarizations for incident light has been performed.^{27,28} We are considering the incident sunlight completely unpolarized, however, inside DSSC structure each light polarized component has its own proper behavior, which is recorded by each

polarized reflectance, transmittance, and absorptance. In this sense, our model includes the effect of the polarization of light by the DSSC structure. However, in our experiments, we are not using polarizer devices to discriminate the detection for each polarized component. Therefore, our model has been adapted for a total reflectance, transmittance, and absorptance with 50% contribution from each polarization

$$R = 0.5R_s + 0.5R_p; \quad T = 0.5T_s + 0.5T_p; \quad A = 0.5A_s + 0.5A_p. \quad (9)$$

The calculations of the energetic quantities using the Poynting theorem (PT), as well as their imaginary transformation to solve a multiscale problem in M matrices, can be found in Sec. 6.

Finally, because the above TMM model describes coherent propagation of light, internal reflections within the thick glass substrate layers leads to narrow spectral oscillations in the calculated transmittance and reflectance spectra,^{18,29} the period of which depends on the ratio of the wavelength and the layer thickness. These oscillations are not seen in the experimental data due to limited spectral resolution or bandwidth of the spectrophotometer, variations in the layer thickness, roughness of the surfaces and interfaces, or the layer thickness exceeding the coherence length of the incident light, which can produce partially coherent or even completely incoherent situation.^{29,30} These oscillations were removed from the calculated data with a moving average filter that was optimized to sufficiently attenuate coherent oscillations originating from the glass layers, while preserving the main spectral features in the main wavelength region of interest (450 to 700 nm), which was adequate due to the large thickness difference between the glass substrates and the other layers in the structure. Other methods presented in the literature for treating incoherent or partially coherent layers in an otherwise coherent optical stack include generalized TMM methods,^{29,31–33} treating the incoherent layers separately with correction factors,^{34,35} or randomizing and averaging the coherent calculations with respect to layer thickness or phase shift,^{36–39} each method giving usually similar results but differ in computational complexity.

2.5 Model Parameters

The refractive indices and layer thicknesses corresponding to the device structures of Fig. 1 are given in Table 1 and Fig. 3. The 1DPC-DSSC has the same structure and properties as the DSSC used for reference but has between its photoelectrode and electrolyte layers a 1DPC made of four porous bilayers of SiO₂ (thickness 80 nm and porosity 45%) and TiO₂ (thickness 100 nm,

Table 1 Refractive indices, thicknesses, and components for the different layers of the DSSC and 1DPC-DSSC for the wavelength range 400 to 800 nm. The spectral refractive indices without a value in this table are represented as wavelength-dependent data in Fig. 3.

Layer j	Components	Real refractive index $n_j(\lambda)$	Imaginary refractive index $\kappa_j(\lambda)$	Thickness d
1	Glass	1.51	$\kappa_1(\lambda)$	3 mm
2	fluorine-doped tin oxide (FTO)	1.81	$\kappa_2(\lambda)$	400 nm
3	Photoelectrode = dyed TiO ₂ (50%) + electrolyte solution (50%)	1.92	$\kappa_3(\lambda)$	5 μ m
1DPC stack	Dyed SiO ₂ (55%) + electrolyte solution (45%)	1.43	$\kappa_3(\lambda)$	80 nm
(4× SiO ₂ /TiO ₂)	Dyed TiO ₂ (42%) + electrolyte solution (58%)	1.81	$\kappa_3(\lambda)$	100 nm
4	Electrolyte solution	1.42	$\kappa_4(\lambda)$	30 μ m
5	Platinum	$n_5(\lambda)$	$\kappa_5(\lambda)$	2 nm
6	FTO	1.81	$\kappa_2(\lambda)$	400 nm
7	Glass	1.51	$\kappa_1(\lambda)$	3 mm

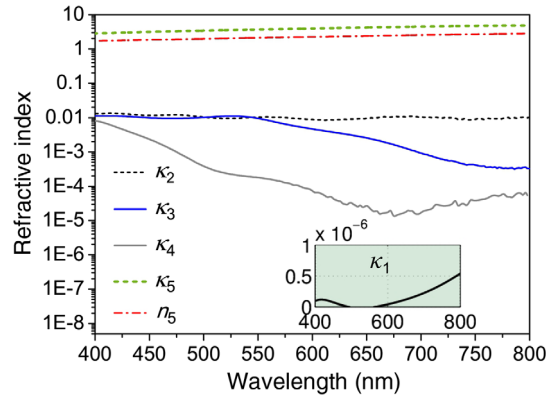


Fig. 3 Spectral refractive indices represented for the DSSC and 1DPC-DSSC (see Table 1).

porosity 58%) infiltrated with electrolyte. The complex refractive indices $\tilde{n}_j(\lambda) = n_j(\lambda) + i\kappa_j(\lambda)$ for each layer were determined experimentally or estimated from the literature. The incoming and outgoing semi-infinite media are both air with $n_0(\lambda) \equiv 1$.

Lynch and Hunter⁴⁰ supplied us both the imaginary and real refractive indices of platinum. The real refractive indices of glass, FTO, electrolyte (considered as pure electrolyte solvent, 3-methoxypropionitrile), and the photoelectrode (considered as a mixture of TiO₂ and the electrolyte solvent) were estimated.^{13,18,41}

The imaginary refractive indices of glass, FTO, electrolyte, and the photoelectrode were obtained experimentally by measuring the normal incidence transmittance of simplified device structures, which had only one unknown layer (e.g., air/glass/electrolyte/glass/air). The absorption coefficient of the unknown layer was determined by analyzing the data with either the TMM model (Sec. 2.3) or a simplified incoherent optical model. The solid layers (glass, FTO, and Pt) were measured in contact with the electrolyte solvent (3-MPN) to establish similar reflectance at the solid/liquid interface as in the complete solar cell. Also the photoelectrode was measured this way to minimize possible solvatochromic effects on the dye.^{42,43}

The photoelectrode was treated as an effective medium consisting of a porous nanocrystalline TiO₂ film (porosity $P \approx 50\%$) with the dye molecules (N719) adsorbed as a monolayer on its surface and the pores volume filled with the electrolyte. The effective complex refractive index $\tilde{n}_3(\lambda)$ of photoelectrode layer was calculated with the Bruggeman's effective medium approximation^{41,44}

$$P \frac{[n_{3M}(\lambda) + i\kappa_{3E}(\lambda)]^2 - \tilde{n}_3^2(\lambda)}{[n_{3M}(\lambda) + i\kappa_{3E}(\lambda)]^2 + 2\tilde{n}_3^2(\lambda)} + (1 - P) \frac{[n_{3T}(\lambda) + i\kappa_{3D}(\lambda)]^2 - \tilde{n}_3^2(\lambda)}{[n_{3T}(\lambda) + i\kappa_{3D}(\lambda)]^2 + 2\tilde{n}_3^2(\lambda)} = 0, \quad (10)$$

where $n_{3M}(\lambda)$ and $n_{3T}(\lambda)$ are the real parts of the refractive indices of the electrolyte solvent (3-methoxypropionitrile) and TiO₂, respectively, and $\kappa_{3E}(\lambda)$ and $\kappa_{3D}(\lambda)$ are the imaginary parts of the refractive indices of the electrolyte and dye, respectively. The approximation Eq. (10) provides the unknown dye imaginary refractive index, as well as the total photoelectrode refractive index $\tilde{n}_3(\lambda) = [n_{3M}(\lambda) + n_{3T}(\lambda)] + i[\kappa_{3E}(\lambda) + \kappa_{3D}(\lambda)]$.

3 Results and Discussion

3.1 Measured and Calculated Transmittance

Figure 4(a) shows measured transmittance spectra of a 1DPC-DSSC and a reference device (DSSC) without the photonic-crystal back-reflector. Both devices show smooth spectra that evolve systematically when the incidence angle increases from 0 deg to 50 deg. Consistent with the theory, the measured transmittance data of the two devices overlap around 750 nm wavelength. According to theoretical calculations discussed later [Fig. 5(b)], the reflectance of the 1DPC is expected to be insignificant in this wavelength region, and hence its influence on the

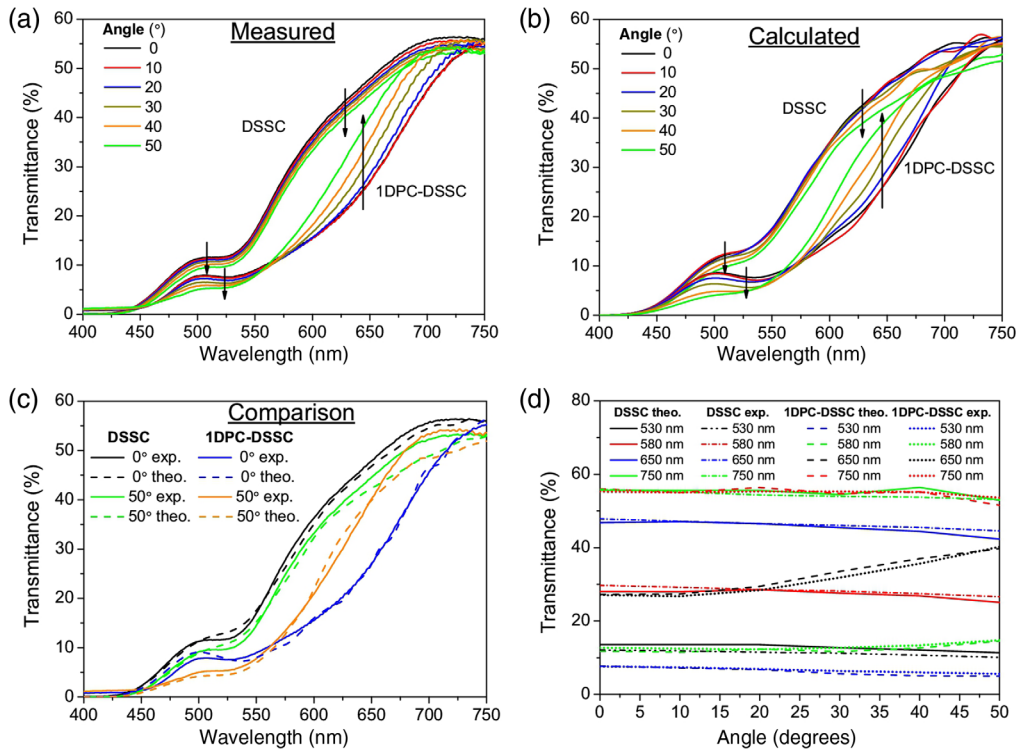


Fig. 4 (a) Measured and (b) calculated transmittance of DSSC and 1DPC-DSSC for incident angles (from air) ranging from 0 deg to 50 deg. (c) Comparison of the measured (experimental) and calculated (theoretical) transmittance of the two types of devices at 0-deg to 50-deg incident angle. The black arrows indicate evolution trends in the spectra as the incidence angle of light is increased. (d) Transmittance as a function of incident angle at wavelengths 530, 580, 650, and 750 nm corresponding to the data presented in (b), as well as comparison between calculated and experimental transmittance.

device transmittance should be small, as observed in the measurements. As expected, the 1DPC-DSSC has substantially lower transmittance than the DSSC reference device, because the 1DPC layer reflects light back to the photoelectrode layer, making the device less transparent.

The added 1DPC decreases the device transmittance over the whole measured spectral range, except at the longest wavelengths, where the effect is, furthermore, angle-dependent: at normal incidence, transmittance decrease is observed up to ca., 750 nm, but at 50 deg only up to 675 nm. A corresponding angle-dependent blue shift of the transmittance spectra appears with 1DPC-DSSC at wavelengths above ca., 575 nm. Also these features are well-explained by the theoretical calculations: when the incidence angle increases, the reflectance peak of the 1DPC shifts to shorter wavelengths [Fig. 5(b)], making the device increasingly transparent at the longer wavelengths. The angle-dependence of the DSSC transmittance is on the contrary much subtler, showing only small, nearly wavelength-independent decrease with increasing angle, which comes mainly from the Fresnel reflection at the air–glass interface of the photoelectrode substrate.

The above-mentioned results agree well also with the previous experiments reported in the literature. Similar overall decreases of device transmittance by 1DPC were seen in several studies.^{4,5,12,13,15,45} Also the angular behavior of the 1DPC-DSSC seen here is in good qualitative agreement with the angular transmittance of the similar red-light-reflecting 1DPC-DSSC measured by López-López et al.,¹³ who also saw similar weakly wavelength-dependent transmittance decrease in their reference DSSC.

Theoretical calculations with the TMM model (Sec. 2) reproduce the experimentally observed spectral and angular transmittance characteristics well. The calculated spectra [Fig. 4(b)] show the same qualitative angular trends (indicated by arrows) as found experimentally, but some quantitative differences can be seen, as highlighted by the on-to-one comparison

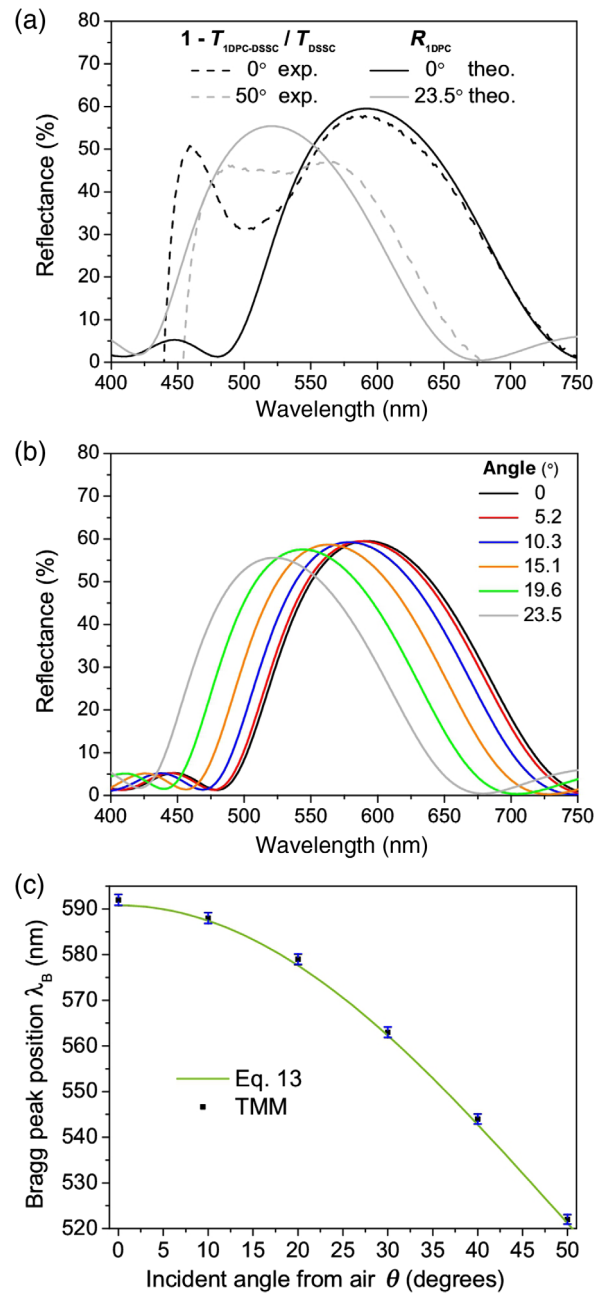


Fig. 5 Theoretical and experimental evaluations of the wavelength and angle-dependent Bragg's reflection peak of the photonic-crystal (1DPC) layer as an internal layer within the 1DPC-DSSC structure. (a) Comparison of the reflectance of the 1DPC layer (R_{1DPC}) calculated with the TMM model for incident light propagating from the photoelectrode layer at 0 deg and 23.5 deg angles (continuous lines), with its experimental estimation calculated with Eq. (11) from the measured transmittance spectra of Fig. 4(a) for the corresponding incident angles of 0 deg and 50 deg from the air (dashed lines). (b) Calculated internal reflectance spectra of the 1DPC (R_{1DPC}) for different incidence angles from the photoelectrode. (c) Angle dependence of the reflectance peak position evaluated from the calculated spectra (b) and from the Bragg's condition [Eq. (13)]. The internal 1DPC reflectance (R_{1DPC}) was calculated by treating the photoelectrode layer (without absorption) as the incoming external medium and the electrolyte (without absorption) as the outgoing external medium. The incident angles from the photoelectrode layer [see the legend in (b)] were calculated by Snell's law considering the incidence angles 0 deg, 10 deg, 20 deg, 30 deg, 40 deg, and 50 deg from air.

of the measured and calculated data in Fig. 4(c). At normal incidence (black and blue lines), the quantitative mismatch between the calculations (dash line) and the measurements (continuous line) is less than ca., 2% units, which is a typical experimental uncertainty in spectrophotometric transmittance measurements. Larger mismatch is observed at 50-deg incidence in the wavelength region 650 to 750 nm [Fig. 4(c)], where the calculated transmittance drops up to ca., 6% units below the measured data. This discrepancy comes most likely from weak light scattering in the 1DPC multilayer, which becomes visible in the experimental data at the wavelengths where the dye absorbs weakly.

3.2 Reflectance of the Photonic-Crystal Layer in 1DPC-DSSC

Since we aim for predictive design of 1DPC-DSSCs, an obvious question to ask here is whether the measured effects of the 1DPC [Fig. 4(a)] can be fully explained by the spectral reflectance of the added 1DPC layer. After all, intense, wavelength-selective reflectance is the main characteristic of 1DPCs and the motivation for their use in DSSCs as back reflector. The good agreement between measured and calculated transmittance discussed above shows already that the TMM model can predict the optical properties of the 1DPC-DSSC reasonably well based on the geometrical and optical properties of the device (layer structure and complex refractive indices, respectively) and is, therefore, suitable for predictive design of 1DPC-DSSCs. Indeed, as already mentioned, TMM is the method of choice for optical modeling of nonlight scattering 1-D multilayers, since it gives an exact theoretical description of the interaction of electromagnetic radiation with the stratified media, in a mathematical form that is well suited for numerical computations, as discussed in Sec. 2.

Although the good match between theory and experiment for the whole-device transmittance is sufficient experimental verification of the optical model, some additional physical insight can be gained by considering also the inverse problem, namely: is it possible to deduce the reflectance spectrum of the 1DPC structure, and further, the structural details of the 1DPC layers, from the measured transmittance difference between the two types of devices? Such information would be useful in practical research and development of photonic-crystal-based devices. In the following, we present a simple approach suitable for quick analysis of experimental results.

If multiple internal reflection of light is negligible in the whole device structure, except within the 1DPC itself, the device transmittance can be approximated as the product of the transmittances of the individual layers 1 to 7 (that constitute the reference DSSC) and the added 1DPC (see Fig. 1). If the light absorption by the 1DPC can be additionally neglected, the internal reflectance of the built-in 1DPC can be estimated from the ratio of the measured device transmittances with ($T_{\text{1DPC-DSSC}}$) and without (T_{DSSC}) the photonic crystal, provided that the latter transmittance is sufficiently high (ca., $T_{\text{DSSC}} > 10\%$)

$$R_{\text{1DPC}} \approx 1 - T_{\text{1DPC}} = 1 - \frac{T_{\text{1DPC-DSSC}}}{T_{\text{DSSC}}}, \quad (11)$$

where we have used the approximation $T_{\text{1DPC-DSSC}} \approx T_{\text{1DPC}}T_{\text{DSSC}}$, which holds with the above approximations.

Figure 5(a) shows that this simple approximation agrees remarkably well with the exact TMM calculation of R_{1DPC} . The position, height, and shape of the reflectance peak are also very similar to the one previously measured directly from a 1DPC that had a similar structure and preparation as here.^{18–20} At wavelengths above 550 nm, where the criterion $T_{\text{DSSC}} \geq 10\%$ is fulfilled, the match between Eq. (11) and the theoretical calculation is nearly perfect in the case of normal incidence, and reasonably good at 50-deg incidence. The good correspondence can be rationalized against the underlying assumptions of Eq. (11). The reflectance at the air-glass interface is only 4%, as calculated by the Fresnel's law using the refractive index data of Table 1, and at the other interfaces, the reflectance is even lower (<4%) due to smaller refractive index change. This means that the reflection of light in the 1DPC-DSSC is dominated by the ca., 60% peak reflectance of the 1DPC structure [Fig. 5(a)], and therefore, neglecting multiple reflections in the reference DSSC is a reasonably good approximation for estimating its experimental value. It also makes sense to assume negligible light absorption by the 1DPC since its thickness is only about

1/7 of the photoelectrode layer. The correspondence of Eq. (11) with the TMM calculation is less satisfactory below 550 nm. In this region, the transmittances drop below 10%, which makes the quantitative estimation of R_{1DPC} with Eq. (11) less reliable. The large differences may be caused by weak light scattering in the multilayer structure, the effect of which becomes visible in the analysis by Eq. (11) when T_{DSSC} drops to low values. Further analysis of the experimental data in this spectral region is therefore omitted.

The good match between calculated and experimentally observed 1DPC reflectance motivates closer theoretical analysis of the factors affecting it. Figure 5(b) shows the evolution of the calculated internal reflectance spectra of the 1DPC with angle. The wide and nearly symmetric reflectance peak corresponds to the main resonance of the Bragg reflection from the 1DPC. The three main characteristics of the reflectance peak are its height (intensity), spectral position and width. As the incidence angle is increased, the peak moves to shorter wavelengths (blue shift) its height decreases slightly, but the width stays roughly constant.

The peak position of the Bragg's reflection in the 1DPC-DSSC can be obtained in two ways: it can be extracted from the reflectance spectra calculated with the TMM [Fig. 5(b)] or it can be estimated from the Bragg's condition approximation. The present photonic crystal has two real refractive indices n_{TiO_2} and n_{SiO_2} , and lengths d_{TiO_2} and d_{SiO_2} , which are repeated as a spatial period (unit cell) with length $d = d_{TiO_2} + d_{SiO_2}$. The peak wavelength of the first-order Bragg's reflection λ_B can be easily obtained from the Bragg's condition applied to the unit cell of the photonic crystal

$$2\beta_{TiO_2}d_{TiO_2} + 2\beta_{SiO_2}d_{SiO_2} = 2\pi \quad \Leftrightarrow \quad 2n_{TiO_2}d_{TiO_2} \cos(\theta_{TiO_2}) + 2n_{SiO_2}d_{SiO_2} \cos(\theta_{SiO_2}) = \lambda_B, \quad (12)$$

where θ_{TiO_2} and θ_{SiO_2} are the propagation angles for each layer of the unit cell. Applying Snell's law between the air and the unit cell, $\sin(\theta) = n_{TiO_2} \sin(\theta_{TiO_2}) = n_{SiO_2} \sin(\theta_{SiO_2})$, the Bragg's condition can be expressed as a function of the incident angle θ from the air medium:

$$\lambda_B = 2d_{TiO_2} \sqrt{(n_{TiO_2})^2 - \sin^2(\theta)} + 2d_{SiO_2} \sqrt{(n_{SiO_2})^2 - \sin^2(\theta)}. \quad (13)$$

Figure 5(c) shows that this simple approximation gives peak positions that are in excellent agreement with those evaluated from the numerically calculated reflectance spectra. This is expected because the Bragg's condition of Eq. (13) is a case of the more general calculation for the Bragg's peak position, which is included in our TMM model. Indeed, Eq. (13) is exact for the condition $d_{TiO_2}n_{TiO_2} \cos(\theta_{TiO_2}) - d_{SiO_2}n_{SiO_2} \cos(\theta_{SiO_2}) = 0$, which corresponds to an omnidirectional dielectric mirror for a bandwidth. The exact analytical-numerical procedure to calculate the Bragg's peak position can be found in Ref. 46.

3.3 Enhancement of the Absorptance by the 1DPC Layer

The purpose of the porous 1DPC layer is to reflect the light that is not absorbed in the photoelectrode in a single pass, and thereby increases the optical path length and absorption in it. The increased light absorption is clearly visible both in the calculated absorptance of the solar cells and in the absorptance by the dye, which is also known as light harvesting efficiency [Figs. 6(a) and 6(b)]. However, compared to the reflectance spectra of the 1DPC layer, which show a clear angle-dependent peak [Fig. 5(b)], the absorptance enhancement by the 1DPC is almost independent of the angle and is more emphasized toward the long wavelengths [Fig. 6(c)]. This can be expected, because the relative absorptance enhancement depends not only on the reflectance of the 1DPC (R_{1DPC}), i.e., the fraction of light reflected, but also on the transmittance of the photoelectrode layer (T_3), i.e., the fraction of light reaching the 1DPC. Obviously, if the photoelectrode layer absorbs all light in a single pass, none will reach the 1DPC. Following the same approximations that led to Eq. (11), namely that light absorption by the 1DPC layer and reflectance at the other interfaces are negligible, the relative enhancement in the absorptance by the dye (A_{dye}) is approximately

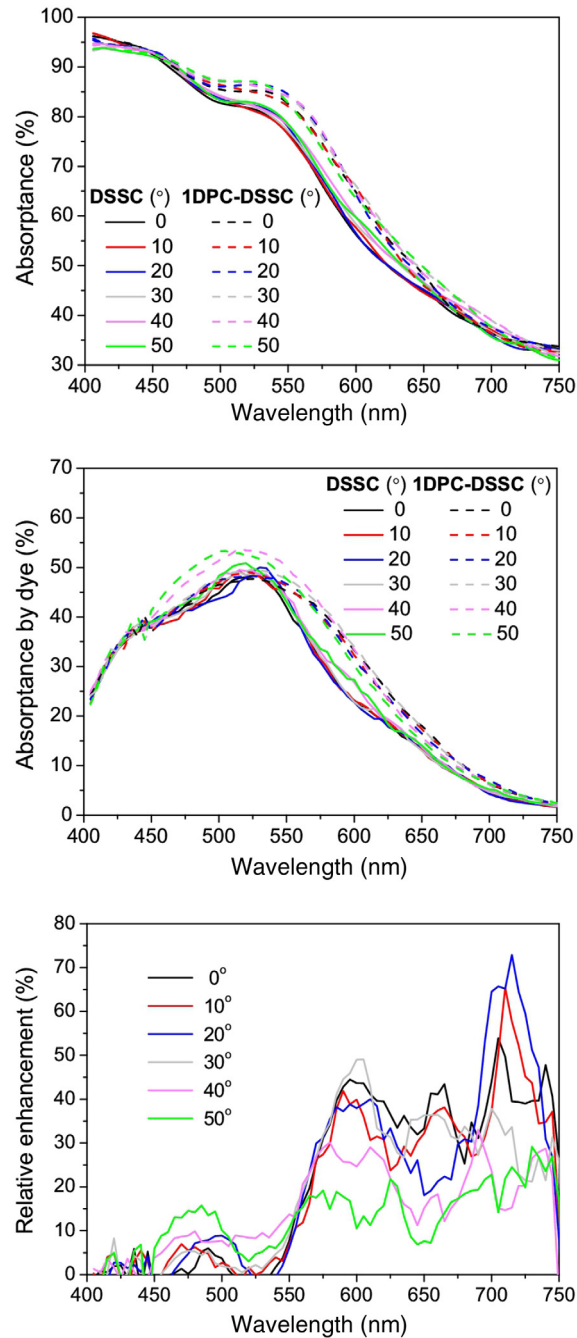


Fig. 6 Calculated (a) total absorbance of the device, (b) the absorbance by the dye in the photoelectrode for DSSC and 1DPC-DSSC, and (c) the relative enhancement in dye absorbance caused by the photonic crystal and calculated with Eq. (14).

$$\frac{A_{\text{dye,1DPC-DSSC}}}{A_{\text{dye,DSSC}}} - 1 \approx T_3 R_{1\text{DPC}}, \quad (14)$$

where we have used the approximations $A_{\text{dye,DSSC}} \approx T_1 T_2 A_3 \frac{\kappa_{3D}}{\kappa_{3E} + \kappa_{3D}}$ and $A_{\text{dye,1DPC-DSSC}} \approx T_1 T_2 A_3 \frac{\kappa_{3D}}{\kappa_{3E} + \kappa_{3D}} (1 + T_3 R_{1\text{DPC}})$, where the numbers in the subscript refer to the layers in Fig. 1.

We can therefore expect to see the maximum relative enhancement at wavelengths where the photoelectrode absorbs weakest (its transmittance T_3 is highest) and the 1DPC reflects most ($R_{1\text{DPC}}$ is highest). More relevant to the photocurrent generation is however the absolute enhancement, which Eq. (14) gives as

$$A_{\text{dye,1DPC-DSSC}} - A_{\text{dye,DSSC}} \approx T_3 R_{\text{1DPC}} A_{\text{dye,DSSC}} \quad (15)$$

The last approximation, which assumes high transmittance through the FTO-glass substrate and weak light absorption by the electrolyte in the pores of the photoelectrode, highlights the fact that the absolute enhancement is small when the absorptance is either high or low ($A_{\text{dye,DSSC}}$ is low and T_3 is high, or *vice versa*) and has a maximum somewhere between these extremes ($A_{\text{dye,DSSC}} \approx 1 - T_3 \approx 50\%$). The result in Fig. 6 follows these expectations well: The biggest absolute enhancement occurs in the intermediate wavelengths (550 to 650 nm) where R_{1DPC} is highest (at normal incidence) and the absorptance by the dye ranges from 45% at 550 nm to 15% at 650 nm [Fig. 6(b)]. Also the relative enhancement is largest above 550 nm [Fig. 6(c)].

Interestingly, the total absorptance of the 1DPC-DSSC is almost independent of the angle [Fig. 6(a)], whereas the absorptance by the dye (light harvesting efficiency) shows angle-dependence in the 450- to 550-nm range in the same 1DPC-DSSC [Fig. 6(b)]. There are several factors behind this result. First, below 550 nm, strong absorption by both the electrolyte and the dye attenuates the absorption enhancement by the 1DPC in the complete device, effectively masking its angular effects. On the other hand, the angular effects are visible in the dye absorptance [Fig. 6(b)], because parasitic absorption by the other layers have been removed in it. Second, as the incidence angle is increased, the 1DPC reflectance decreases above 575 nm [Fig. 5(b)], but its effect on the total absorptance is compensated by increase in the optical path length through the semitransparent device.

4 Experimental Section

4.1 Materials and Preparation

The solar cells were prepared as reported before.¹³ Briefly, 5- μm -thick TiO_2 photoelectrodes of 0.25 cm^2 area were prepared by screen printing 18-NRT paste (Dyesol[®]) on FTO glass (TEC 11 $\Omega/\text{sq.}$, Nippon Sheet Glass) followed by sequential heating for 15 min at 180°C, 15 min at 450°C, and 15 min at 500°C. The 1DPC structures were prepared by spin coating eight alternating layers of SiO_2 and TiO_2 nanoparticle suspensions on the photoelectrodes [see Fig. 1(b)]. The SiO_2 particles with average size of 30 nm were obtained from Dupont (34 wt. % in H_2O , LUDOX[®] TMA) and the TiO_2 particles (average size of 6 nm) were synthesized following a previously reported procedure.⁴⁷ For the spin coating, both types of particles were suspended in a mixture of water (21 vol%) and methanol (79 vol%). The particle concentrations used in the suspensions were 2 wt. % for SiO_2 and 5 wt. % for TiO_2 . The TiO_2 suspension included also porosity controlling polymer (PEG 20000, Fluka, wt. ratio PEG: TiO_2 = 0.5) that was removed after each TiO_2 /PEG deposition with heat treatment (300°C 15 min) to create larger pores in the TiO_2 layer. Finally, the samples were annealed at 450°C for 30 min to mechanically stabilize the multilayer.

For dye-sensitization, the photoelectrodes were first dried at 120°C for 3 h, then soaked overnight into a 0.2-mM solution of N719 dye (Solaronix[®]) in ethanol, followed by rinsing with ethanol and drying at room temperature. Counter electrodes were prepared by drop-casting colloidal platinum solution (Platisol T, Solaronix[®]) onto an FTO glass and heating at 400°C for 15 min. Solar cells were assembled by sealing the electrodes together with a thermopolymer frame (Surlyn 30, Dyesol[®]), and filling with liquid electrolyte through two holes made previously on the counter electrode. The electrolyte composition was 100 mM I_2 (Aldrich, 99.999%), 100 mM LiI (Aldrich, 99.9%), 600 mM [(C4H9)4N]I (Aldrich, 98%), and 500 mM 4-tert-butylpyridine (Aldrich, 99%), using 3-methoxy propionitrile (Fluka, $\geq 99\%$) as a solvent.

Reference DSSCs were made using TiO_2 electrodes of the same thickness but without including the 1DPC structure.

4.2 Transmittance Measurements

Transmittance spectra of the solar cells were measured with an UV scanning spectrophotometer (SHIMADZU UV-2101PC). The light incident on the solar cells formed the photoelectrode side

and focused inside the active area of the photoelectrode. Angular measurements were taken using a sample holder attached to a rotating stage that had an angular scale with resolution of 10 arc min.

4.3 Numerical Calculations

The numerical calculations of the TMM model describe above were performed using MATLAB version 7.11.0.584 (R2010b) software and an Intel Xeon CPU E3-1230 at 3.20 GHz processor.

5 Conclusions

We reported a theoretical model based on TMM for the analysis of the coherent angular optics of DSSC employing an internal porous 1DPC back reflector. The model completes our earlier model development^{19,20} and includes special measures to avoid numerical instabilities that would otherwise occur in the case of thick, strongly absorbing layers. Using independent-refractive index data obtained from the literature and separate optical characterization of the used materials, the model produced results in excellent quantitative agreement with angle-dependent transmittance spectra recorded from complete DSSCs, verifying the validity and practical applicability of the model for this purpose. Further analysis of the data showed that the ratio of device transmittance measured with and without a 1DPC yields quantitative information on the internal reflectance spectrum of the 1DPC layer, providing a simple and practical method for its indirect evaluation. The model reported here provides an accurate optical description of the angular characteristics of DSSCs and their possible internal photonic-crystal reflector in the case when light scattering in the device structure is negligible.

6 Appendix A: Energetic Calculations Using Poynting Theorem

The squared electric field of the interaction system is defined as $\text{Re}[\tilde{\mathbf{E}}_j(\mathbf{r}, t)] \cdot \text{Re}[\tilde{\mathbf{E}}_j(\mathbf{r}, t)]$, which has a time-average defined by

$$\begin{aligned} & \langle \text{Re}[\tilde{\mathbf{E}}(\mathbf{r}, t)] \cdot \text{Re}[\tilde{\mathbf{E}}(\mathbf{r}, t)] \rangle_t \\ &= \frac{\omega}{2\pi} \int_{-\pi/\omega}^{+\pi/\omega} \text{Re}[\tilde{\mathbf{E}}(\mathbf{r}) \cdot \tilde{\mathbf{E}}^*(\mathbf{r})] dt + \frac{\omega}{2\pi} \int_{-\pi/\omega}^{+\pi/\omega} \text{Re}[\tilde{\mathbf{E}}(\mathbf{r}) \cdot \tilde{\mathbf{E}}(\mathbf{r}) e^{2i\omega t}] dt = |\tilde{\mathbf{E}}(\mathbf{r})|^2, \end{aligned} \quad (16)$$

the fully stable electric field [Eqs. (3) and (4)] from article can be introduced in Eq. (16) providing the squared electric field as

$$|\tilde{\mathbf{E}}(\mathbf{r})|^2 = \begin{cases} [e^{2\text{Im}(\tilde{\beta}_0)(y-y_0)} + |\tilde{E}_0^-|^2 e^{-2\text{Im}(\tilde{\beta}_0)(y-y_0)} + 2\text{Re}\{\tilde{E}_0^- e^{-i2\text{Re}(\tilde{\beta}_0)(y-y_0)}\}] e^{2\text{Im}(\tilde{\alpha})(x-x_0)} \\ \quad \text{with } y \in (-\infty, y_0); \quad x \in (x_0, +\infty) \\ [|\tilde{E}_j^+|^2 e^{2\text{Im}(\tilde{\beta}_j)(y-y_{j-1})} + |\tilde{E}_j^-|^2 e^{-2\text{Im}(\tilde{\beta}_j)(y-y_{j-1})} + 2\text{Re}\{\tilde{E}_j^+ \tilde{E}_j^- e^{-i2\text{Re}(\tilde{\beta}_j)(y-y_0)}\}] e^{2\text{Im}(\tilde{\alpha})(x-x_0)} \\ \quad \text{with } y \in (y_{j-1}, y_j); \quad x \in (x_0, +\infty) \end{cases} \quad (17)$$

where $j = 1, \dots, n+1$; with the amplitude conditions $\tilde{E}_{n+1}^- = 0$, $\tilde{E}_0^+ = 1$ and with $y_{n+1} = +\infty$. Equation (17) shows three types of spatial exponential terms: the first is a decreasing forward wave, the second is an increasing backward wave, and the third is an oscillating forward-backward interference. Note that squared electric field Eq. (17) depends implicitly on the polarization modes through the amplitude coefficients, which are calculated with the \mathbf{D} -matrices of Eq. (2) from article. Therefore, the total squared electric field has the independent contributions from both modes such as $|\tilde{\mathbf{E}}(\mathbf{r})|_{\text{total}}^2 = |\tilde{\mathbf{E}}^s(\mathbf{r})|^2 + |\tilde{\mathbf{E}}^p(\mathbf{r})|^2$.

PT provides power flux and power absorption rate through the interaction system. The Poynting vector projection along one spatial direction provides these quantities through that

direction. Therefore, the time-average power flux along the $\hat{\mathbf{y}}$ direction (see from article Fig. 2), is given by

$$\begin{aligned} \langle \mathbf{S}(\mathbf{r}, t) \cdot \hat{\mathbf{y}} \rangle &= \frac{\omega}{4\pi} \int_{-\pi/\omega}^{+\pi/\omega} \{ \text{Re}[\tilde{\mathbf{E}}_j(\mathbf{r}) \times \tilde{\mathbf{H}}_j^*(\mathbf{r})] \} \cdot \hat{\mathbf{y}} dt \\ &\quad + \frac{\omega}{4\pi} \int_{-\pi/\omega}^{+\pi/\omega} \{ \text{Re}[\tilde{\mathbf{E}}_j(\mathbf{r}) \times \tilde{\mathbf{H}}_j(\mathbf{r}) e^{2i\omega t}] \} \cdot \hat{\mathbf{y}} dt \\ &= \frac{1}{2} \text{Re}[\tilde{\mathbf{E}}_j(\mathbf{r}) \times \tilde{\mathbf{H}}_j^*(\mathbf{r})] \cdot \hat{\mathbf{y}}, \quad \text{where } j = 0, 1, \dots, n+1, \end{aligned} \quad (18)$$

where power flux units are given in W/m^2 when electric field $\tilde{\mathbf{E}}_j(\mathbf{r})$ and magnetic field $\tilde{\mathbf{H}}_j(\mathbf{r})$ are given in V/m and A/m , respectively. Note that the magnetic can be easily evaluated from the electric field using Maxwell's equations. The time-average power flux along the $\hat{\mathbf{y}}$ direction given by Eq. (18) is analytically evaluated as

$$\begin{aligned} \langle \mathbf{S}(\mathbf{r}, t) \cdot \hat{\mathbf{y}} \rangle &= \begin{cases} \frac{1}{2c} \text{Re}\{\tilde{n}_0^* \cos^*(\tilde{\theta}_0)\} [-e^{2\text{Im}\tilde{\beta}_0(y-y_0)} + |\tilde{E}_0^-|^2 e^{-2\text{Im}\tilde{\beta}_0(y-y_0)} \\ \quad + 2i \text{Im}\{\tilde{E}_0^- e^{-2i\text{Re}\tilde{\beta}_0(y-y_0)}\}] e^{2\text{Im}\tilde{\alpha}(x-x_0)} & \text{with } y \in (-\infty, y_0); \quad x \in (x_0, +\infty) \\ \frac{1}{2c} \text{Re}\{\tilde{n}_j^* \cos^*(\tilde{\theta}_j)\} [-|\tilde{E}_j^+|^2 e^{2\text{Im}\tilde{\beta}_j(y-y_{j-1})} + |\tilde{E}_j^-|^2 e^{-2\text{Im}\tilde{\beta}_j(y-y_{j-1})} \\ \quad + 2i \text{Im}\{\tilde{E}_j^+ \tilde{E}_j^- e^{-2i\text{Re}\tilde{\beta}_j(y-y_{j-1})}\}] e^{2\text{Im}\tilde{\alpha}(x-x_0)} & \text{with } y \in (y_{j-1}, y_j); \quad x \in (x_0, +\infty), \end{cases} \end{aligned} \quad (19)$$

where $j = 1, \dots, n+1$; with $\tilde{E}_{n+1}^- = 0$, $\tilde{E}_0^+ = 1$, and $y_{n+1} = +\infty$. The power flux along the $\hat{\mathbf{y}}$ direction of Eq. (19) has implicit both polarizations, which gives a total power flux $\langle \mathbf{S}(\mathbf{r}, t) \cdot \hat{\mathbf{y}} \rangle_{\text{total}} = \langle \mathbf{S}(\mathbf{r}, t) \cdot \hat{\mathbf{y}} \rangle_s + \langle \mathbf{S}(\mathbf{r}, t) \cdot \hat{\mathbf{y}} \rangle_p$ when is normalized to a total incident power flux of $1 \text{ W}/\text{m}^2$ for all wavelength. The power flux in Eq. (19) contains the terms: decreasing forward flux, increasing backward flux, as well as an interaction term.

The power flux lost in the spatial interval of the multilayer (y_a, y_b) corresponds to the absorption inside that interval, if we guess that there is not scattering radiation, which is evaluated such as

$$\langle \mathbf{S}(\mathbf{r}, t) \cdot \hat{\mathbf{y}} \rangle|_{(y_a, y_b)} = \langle \mathbf{S}(\mathbf{r}, t) \cdot \hat{\mathbf{y}} \rangle|_{y=y_a} - \langle \mathbf{S}(\mathbf{r}, t) \cdot \hat{\mathbf{y}} \rangle|_{y=y_b} \quad (20)$$

dividing Eq. (20) between the interval (y_a, y_b) and taking the limit where interval length goes to zero, it is obtained the power absorption rate per volume along $\hat{\mathbf{y}}$ direction, which is defined as

$$\begin{aligned} \frac{d}{dy} \langle \mathbf{S}(\mathbf{r}, t) \cdot \hat{\mathbf{y}} \rangle &= \begin{cases} -\frac{1}{c} \text{Re}\{\tilde{n}_0^* \cos^*(\tilde{\theta}_0)\} \text{Im}\{\tilde{\beta}_0\} [e^{2\text{Im}\tilde{\beta}_0(y-y_0)} + |\tilde{E}_0^-|^2 e^{-2\text{Im}\tilde{\beta}_0(y-y_0)}] e^{2\text{Im}\tilde{\alpha}(x-x_0)} \\ \quad - \frac{2}{c} \text{Re}\{\tilde{n}_0^* \cos^*(\tilde{\theta}_0)\} i \text{Im}\{i \tilde{E}_0^- \text{Re}(\tilde{\beta}_0) e^{-2i\text{Re}\tilde{\beta}_0(y-y_0)}\} e^{2\text{Im}\tilde{\alpha}(x-x_0)}; \\ \quad \text{with } y \in (-\infty, y_0); \quad x \in (x_0, +\infty) \\ -\frac{1}{c} \text{Re}\{\tilde{n}_j^* \cos^*(\tilde{\theta}_j)\} \text{Im}\{\tilde{\beta}_j\} [|\tilde{E}_j^+|^2 e^{2\text{Im}\tilde{\beta}_j(y-y_{j-1})} + |\tilde{E}_j^-|^2 e^{-2\text{Im}\tilde{\beta}_j(y-y_{j-1})}] e^{2\text{Im}\tilde{\alpha}(x-x_0)} \\ \quad - \frac{2}{c} \text{Re}\{\tilde{n}_j^* \cos^*(\tilde{\theta}_j)\} i \text{Im}\{i \tilde{E}_j^+ \tilde{E}_j^- \text{Re}(\tilde{\beta}_j) e^{-2i\text{Re}\tilde{\beta}_j(y-y_{j-1})}\} e^{2\text{Im}\tilde{\alpha}(x-x_0)}; \\ \quad \text{with } y \in (y_{j-1}, y_j); \quad x \in (x_0, +\infty), \end{cases} \end{aligned} \quad (21)$$

where total power absorption rate is given as $d/dy \langle \mathbf{S}(\mathbf{r}, t) \cdot \hat{\mathbf{y}} \rangle_{\text{total}} = d/dy \langle \mathbf{S}(\mathbf{r}, t) \cdot \hat{\mathbf{y}} \rangle_s + d/dy \langle \mathbf{S}(\mathbf{r}, t) \cdot \hat{\mathbf{y}} \rangle_p$. The quantities defined above characterize the optic-energetic behavior of a multilayer device like a DSSC.

Equations (17), (19), and (21) are obtained with the new stable representation of the TMM, which avoids the numerical problems of inversion in the propagation matrices.²⁰ Nevertheless, this new stable TMM representation is expanded in some coefficient scales given by the matrices \mathbf{M}_j^+ . Therefore, one same calculation could include multiple different magnitude scale orders, where each magnitude order is well-resolved by itself but cannot be compared, in the same calculation, with some other magnitude orders. This clearly represents a multiscale numerical problem, which is magnified by the coupling of a pair of electromagnetic fields, such as in the calculation of Eqs. (17), (19), and (21). The multiscale problem generates as a cut-off at some scale in the computer numerical calculation of these last quantities. For this reason, an increase of significant digits in calculations could avoid this multiscale problem. Indeed, the right calculation at multiple scales can be recovered by introducing an imaginary transformation in the complex-plane, which is designed as a very small oscillatory component,⁴⁸ in Eqs. (17), (19), and (21), giving this complex-plane transformation of the new relations:

$$\begin{aligned} |\tilde{\mathbf{E}}(\mathbf{r})|^2 &\rightarrow |\tilde{\mathbf{E}}(\mathbf{r})|^2 \pm i\varepsilon \\ \langle \mathbf{S}(\mathbf{r}, t) \cdot \hat{\mathbf{y}} \rangle &\rightarrow \langle \mathbf{S}(\mathbf{r}, t) \cdot \hat{\mathbf{y}} \rangle \pm i\varepsilon \\ \frac{d}{dy} \langle \mathbf{S}(\mathbf{r}, t) \cdot \hat{\mathbf{y}} \rangle &\rightarrow \frac{d}{dy} \langle \mathbf{S}(\mathbf{r}, t) \cdot \hat{\mathbf{y}} \rangle \pm i\varepsilon \end{aligned}$$

where $\varepsilon \in \mathfrak{R}$, $|\varepsilon| \ll 1$. (22)

Therefore, the multiscale problem can be handled using the complex perturbation $\pm i\varepsilon$, which represents a constant small translational transformation of Eqs. (17), (19), and (21). This is a very important result since until now the conventional TMM has been used only for complete calculations of thin structures, i.e., in the length order of millimeters.⁴⁹ We have tailored the complex perturbed equation [Eq. (22)] for a complete calculation for multilayer structures in the length magnitude order of meters.

Acknowledgments

The authors thank Hernán Míguez for fruitful discussions during the work. This work was partially funded by the Nordic Innovation Center project, NORDIC DSC (No. 09053) and the CNB-E Project of the Aalto University, Multidisciplinary Institute of Digitalization and Energy.

References

1. N. Martin and J. M. Ruiz, "Calculation of the PV modules angular losses under field conditions by means of an analytical model," *Sol. Energy Mater. Sol. Cells* **70**(1), 25–38 (2001).
2. W. De Soto, S. A. Klein, and W. A. Beckman, "Improvement and validation of a model for photovoltaic array performance," *Sol. Energy* **80**(1), 78–88 (2006).
3. K. Xie, M. Guo, and H. Huang, "Photonic crystals for sensitized solar cells: fabrication, properties, and applications," *J. Mater. Chem. C* **3**(41), 10665–10686 (2015).
4. S. Colodrero et al., "Porous one-dimensional photonic crystals improve the power-conversion efficiency of dye-sensitized solar cells," *Adv. Mater.* **21**(7), 764–770 (2009).
5. L.-P. Heiniger et al., "See-through dye-sensitized solar cells: photonic reflectors for tandem and building integrated photovoltaics," *Adv. Mater.* **25**(40), 5734–5741 (2013).
6. H. J. Park et al., "Photonic color filters integrated with organic solar cells for energy harvesting," *ACS Nano* **5**(9), 7055–7060 (2011).
7. M. E. Calvo, "Materials chemistry approaches to the control of the optical features of perovskite solar cells," *J. Mater. Chem. A* **5**(39), 20561–20578 (2017).
8. K.-T. Lee et al., "Colored ultrathin hybrid photovoltaics with high quantum efficiency," *Light Sci. Appl.* **3**(10), e215 (2014).
9. G. Y. Yoo et al., "Multiple-color-generating Cu(In, Ga)(S, Se)₂ thin-film solar cells via dichroic film incorporation for power-generating window applications," *ACS Appl. Mater. Interfaces* **9**(17), 14817–14826 (2017).

10. V. Nader, S. L. Luxembourg, and A. Polman, "Efficient colored silicon solar modules using integrated resonant dielectric nanoscaters," *Appl. Phys. Lett.* **111**(7), 073902 (2017).
11. J. H. Selj et al., "Reduction of optical losses in colored solar cells with multilayer anti-reflection coatings," *Sol. Energy Mater. Sol. Cells* **95**(9), 2576–2582 (2011).
12. D. Colonna et al., "Introducing structural colour in DSCs by using photonic crystals: interplay between conversion efficiency and optical properties," *Energy Environ. Sci.* **5**(8), 8238–8243 (2012).
13. C. López-López et al., "Angular response of photonic crystal based dye sensitized solar cells," *Energy Environ. Sci.* **6**(4), 1260–1266 (2013).
14. M. Anaya et al., "Resonant photocurrent generation in dye-sensitized periodically nanostructured photoconductors by optical field confinement effects," *J. Am. Chem. Soc.* **135**(21), 7803–7806 (2013).
15. C. López-López, S. Colodrero, and H. Míguez, "Panchromatic porous specular back reflectors for efficient transparent dye solar cells," *Phys. Chem. Chem. Phys.* **16**(2), 663–668 (2014).
16. Y. Li, M. E. Calvo, and H. Míguez, "Integration of photonic crystals into flexible dye solar cells: a route toward bendable and adaptable optoelectronic devices displaying structural color and enhanced efficiency," *Adv. Opt. Mater.* **4**(3), 464–471 (2016).
17. M. E. Calvo et al., "Porous one dimensional photonic crystals: novel multifunctional materials for environmental and energy applications," *Energy Environ. Sci.* **4**(12), 4800–4812 (2011).
18. G. Lozano et al., "Theoretical analysis of the performance of one-dimensional photonic crystal-based dye-sensitized solar cells," *J. Phys. Chem. C* **114**(8), 3681–3687 (2010).
19. J. M. Luque-Raigón et al., "Symmetry analysis of the numerical instabilities in the transfer matrix method," *J. Opt.* **15**(12), 125719 (2013).
20. J. M. Luque-Raigón, J. Halme, and H. Míguez, "Fully stable numerical calculations for finite one-dimensional structures: mapping the transfer matrix method," *J. Quant. Spectrosc. Radiat. Transfer* **134**, 9–20 (2014).
21. K. Yasumoto, *Electromagnetic Theory and Applications for Photonic Crystals*, CRC Press, Boca Raton, Florida (2005).
22. J. D. Joannopoulos, *Photonic Crystals: Molding the Flow of Light*, 2nd edn., Princeton University Press, Princeton (2008).
23. M. Skorobogatiy and J. Yang, *Fundamentals of Photonic Crystal Guiding*, Cambridge University Press, Cambridge (2009).
24. J. D. Jackson, *Classical Electrodynamics*, John Wiley & Sons, Hoboken, New Jersey (1998).
25. M. S. Tomaš, "Green function for multilayers: light scattering in planar cavities," *Phys. Rev. A* **51**(3), 2545–2559 (1995).
26. D. P. Fussell, R. C. McPhedran, and C. M. de Sterke, "Three-dimensional Green's tensor, local density of states, and spontaneous emission in finite two-dimensional photonic crystals composed of cylinders," *Phys. Rev. E* **70**(6), 066608 (2004).
27. A. H. Aly and H. S. Hanafey, "Polarization modes control on the transmittance characteristics of one dimensional photonic crystal," *J. Comput. Theor. Nanosci.* **8**(10), 1916–1919 (2011).
28. A. H. Aly and H. Sayed, "Computer simulation and modeling of solar energy based on photonic band gap materials," *Opt. Appl.* **48**(1), 117–126 (2018).
29. C. C. Katsidis and D. I. Siapkas, "General transfer-matrix method for optical multilayer systems with coherent, partially coherent, and incoherent interference," *Appl. Opt.* **41**(19), 3978–3987 (2002).
30. B. Harbecke, "Coherent and incoherent reflection and transmission of multilayer structures," *Appl. Phys. B Lasers Opt.* **39**(3), 165–170 (1986).
31. E. Centurioni, "Generalized matrix method for calculation of internal light energy flux in mixed coherent and incoherent multilayers," *Appl. Opt.* **44**(35), 7532–7539 (2005).
32. S. Jung et al., "Optical modeling and analysis of organic solar cells with coherent multilayers and Incoherent glass substrate using generalized transfer matrix method," *Jpn. J. Appl. Phys.* **50**(12), 122301 (2011).

33. S. Lee et al., "Effect of incidence angle and polarization on the optimized layer structure of organic solar cells," *Sol. Energy Mater. Sol. Cells* **118**, 9–17 (2013).
34. K. Kang, S. Lee, and J. Kim, "Effect of an incoherent glass substrate on the absorption efficiency of organic solar cells at oblique incidence analyzed by the transfer matrix method with a glass factor," *Jpn. J. Appl. Phys.* **52**(5R), 052301 (2013).
35. M. Young et al., "Angle dependence of transparent photovoltaics in conventional and optically inverted configurations," *Appl. Phys. Lett.* **103**(13), 133304 (2013).
36. G. Y. Margulis et al., "Parasitic absorption and internal quantum efficiency measurements of solid-state dye sensitized solar cells," *Adv. Energy Mater.* **3**(7), 959–966 (2013).
37. K. Kang et al., "A simple numerical modeling of the effect of the incoherent thick substrate in thin-film solar cells based on the equispaced thickness method," *IEEE Photonics J.* **8**(5), 1–12 (2016).
38. M. C. Tropicovsky et al., "Transfer-matrix formalism for the calculation of optical response in multilayer systems: from coherent to incoherent interference," *Opt. Express* **18**(24), 24715–24721 (2010).
39. R. Santbergen, A. H. M. Smets, and M. Zeman, "Optical model for multilayer structures with coherent, partly coherent and incoherent layers," *Opt. Express* **21**(102), A262–A267 (2013).
40. D. W. Lynch and W. R. Hunter, "Comments on the optical constants of metals and an introduction to the data for several metals," in *Handbook of Optical Constants of Solids*, E. D. Palik, Ed., pp. 275–367, Academic Press, Burlington (1997).
41. S. Wenger et al., "Coupled optical and electronic modeling of dye-sensitized solar cells for steady-state parameter extraction," *J. Phys. Chem. C* **115**(20), 10218–10229 (2011).
42. S. G. Boxer, "Stark realities," *J. Phys. Chem. B* **113**(10), 2972–2983 (2009).
43. U. B. Cappel et al., "The influence of local electric fields on photoinduced absorption in dye-sensitized solar cells," *J. Am. Chem. Soc.* **132**(26), 9096–9101 (2010).
44. V. D. Bruggeman, "Berechnung verschiedener physikalischer Konstanten von heterogenen Substanzen. I. Dielektrizitätskonstanten und Leitfähigkeiten der Mischkörper aus isotropen Substanzen," *Ann. Phys.* **416**(7), 636–664 (1935).
45. S. Colodrero et al., "Efficient transparent thin dye solar cells based on highly porous 1D photonic crystals," *Adv. Funct. Mater.* **22**(6), 1303–1310 (2012).
46. S. J. Orfanidis, *Electromagnetic Waves and Antennas* (2016).
47. S. D. Burnside et al., "Self-organization of TiO₂ nanoparticles in thin films," *Chem. Mater.* **10**(9), 2419–2425 (1998).
48. J. P. Boyd, "Complex coordinate methods for hydrodynamic instabilities and Sturm–Liouville eigenproblems with an interior singularity," *J. Comput. Phys.* **57**(3), 454–471 (1985).
49. P. Yeh, *Optical Waves in Layered Media*, Wiley-Interscience, Hoboken, New Jersey (2005).

Biographies of the authors are not available.